



Article

Facile Synthesis of Ordered Mesoporous Orthorhombic Niobium Oxide ($T\text{-Nb}_2\text{O}_5$) for High-Rate Li-Ion Storage with Long Cycling Stability

Ediga Umeshbabu ^{1,2,*}, Divya Velpula ³, Guruprakash Karkera ², Maddukuri Satyanarayana ^{4,*}, Vasudevarao Pasala ⁴ and P. Justin ⁵

¹ Department of Chemistry, Indian Institute of Technology Madras, Chennai 600036, India

² Helmholtz Institute Ulm (HIU) for Electrochemical Energy Storage, Helmholtzstraße 11, D-89081 Ulm, Germany; karkera.guruprakash@uni-ulm.de

³ Center for Nano Science and Technology, Jawaharlal Nehru Technological University Hyderabad, Telangana 500085, India; divya.velpula905@gmail.com

⁴ Amara Raja Batteries Limited, Research and Development, Li-ion Battery Technology, New Energy Storage Technology, Tirupati 517520, India; pvr1@amararaja.com,

⁵ Department of Chemistry, Rajiv Gandhi University of Knowledge Technologies, RK Valley, Kadapa 516330, India; ponjustin@rgukt.in

* Correspondence: umeshediga@gmail.com (E.U.); satya11.iitg@gmail.com (M.S.)

Abstract: Herein, we describe the synthesis and evaluation of hierarchical mesoporous orthorhombic niobium oxide ($T\text{-Nb}_2\text{O}_5$) as an anode material for rechargeable lithium-ion batteries (LIB). The as-synthesized material addresses key challenges such as beneficial porous structure, poor rate capability, and cycling performance of the anode for Li-ion devices. The physicochemical characterization results reveal hierarchical porous nanostructure morphology with agglomerated particles and a 20 to 25 nm dimension range. Moreover, the sample has a high specific surface area ($\sim 65 \text{ m}^2 \text{ g}^{-1}$) and pore volume ($0.135 \text{ cm}^3 \text{ g}^{-1}$). As for the application in Li-ion devices, the $T\text{-Nb}_2\text{O}_5$ delivered an initial discharging capacity as high as 225 mAh g^{-1} at 0.1 A g^{-1} and higher rate capability as well as remarkable cycling features ($\sim 70\%$ capacity retention after 300 cycles at 250 mA g^{-1}) with 98% average Coulombic efficiency (CE). Furthermore, the scan rate-dependent charge storage mechanism of the $T\text{-Nb}_2\text{O}_5$ electrode material was described, and the findings demonstrate that the electrode shows an evident and highly effective pseudocapacitive Li intercalation behaviour, which is crucial for understanding the electrode process kinetics. The origin of the improved performance of $T\text{-Nb}_2\text{O}_5$ results from the high surface area and mesoporous structure of the nanoparticles.

Keywords: niobium pentoxide; nanoparticles; Rietveld refinement; crystal structure; energy storage; Li-ion intercalation; electrochemical performance



Citation: Umeshbabu, E.; Velpula, D.; Karkera, G.; Satyanarayana, M.; Pasala, V.; Justin, P. Facile Synthesis of Ordered Mesoporous Orthorhombic Niobium Oxide ($T\text{-Nb}_2\text{O}_5$) for High-Rate Li-Ion Storage with Long Cycling Stability. *Batteries* **2023**, *9*, 357. <https://doi.org/10.3390/batteries9070357>

Academic Editor: Carolina Rosero-Navarro

Received: 24 May 2023

Revised: 27 June 2023

Accepted: 30 June 2023

Published: 4 July 2023



Copyright: © 2023 by the authors. Licensee MDPI, Basel, Switzerland. This article is an open access article distributed under the terms and conditions of the Creative Commons Attribution (CC BY) license (<https://creativecommons.org/licenses/by/4.0/>).

1. Introduction

The ever-increasing worldwide population and the use of huge quantities of fossil fuel exacerbate environmental pollution challenges, prompting a quest for alternate or renewable energy sources in recent decades [1,2]. Finding an excellent alternative energy system is only part of the problem, whereas creating a suitable energy storage system is essential. For this reason, many energy storage technologies have been researched during the past few years [3–5]. Substantial energy density, high power characteristics, extended cycle lifetime, and superior safety are required for energy storage devices [6,7]. Supercapacitors deliver charges rather quickly because charge storage comprises physical adsorption and desorption of charges on the surface of the electrode materials [8,9]. Supercapacitors, on the other hand, have a low energy density [10,11]. In contrast, most LIBs have large energy densities due to the ability of the bulk structure to hold Li ions and the high operating voltage of the intercalation compounds [12]. However, the slow solid-state Li^+ ion diffusion

in the bulk host structure results in poor power characteristics and significant volume changes during repeated intercalation/extraction procedures, limiting the ability to satisfy current needs [13]. Reducing the size of intercalation-based active materials to the nanoscale improves the cyclability and rate performance of LIBs. The energy properties deteriorate with this method due to the substantial amplification of undesirable side effects in the anodic potential area [14]. Innovative electrode materials and complex designs are required to build enhanced energy storage devices with superior energy and power densities and long cycle lifetimes.

Carbonaceous materials, mainly graphite, have been widely used as anode materials due to their low working voltage, abundant production, and low cost [15]. However, their use in high-energy LIBs is severely limited by their low theoretical capacity and poor rate capability [15,16]. Transition metal oxides (TMO_x ; TM = Fe, Mn, Ni, Co, Sn, Si, Cu, and so on) with high theoretical capacities have recently attracted a lot of interest for anode materials in the next generation of batteries because they provide high Li^+ storage capacities [17,18]. Unfortunately, the Li^+ insertion and reinsertion process causes huge volume expansion and severe particle aggregation, resulting in electrode pulverization and particle contact breaking, leading to considerable capacity loss and poor cycle capability [18]. Lithium titanate ($Li_4Ti_5O_{12}$) is another notable anode material that provides a high charge-discharge voltage of 1.55 V (vs. Li/Li⁺) and extremely stable cycling stability owing to small volume change that occurs during the Li^+ insertion and reinsertion process [19]. However, the poor electronic conductivity, low theoretical capacity (170 mA h g⁻¹), and high working voltage have restricted its practical production. Recently, Nb_2O_5 has been investigated as an appealing anode material for LIBs due to its intercalation pseudocapacitance characteristic, which enables insertion/extraction mechanism for Li ions with an enhanced potential range, preventing the formation of Li dendrites [6,20–22]. The rich redox chemistry of Nb_2O_5 (Nb^{5+}/Nb^{4+} , Nb^{4+}/Nb^{3+}) contributes to high specific capacity [2]. Nb_2O_5 has significant safety benefits because of its suitable working voltage plateau (1.0–2.0 V). Due to its affordability, environmental friendliness, high corrosive resistance, and stability, it is an ideal electrode material in LIBs [21–24].

Furthermore, the electrochemical properties of Nb_2O_5 materials are largely influenced by their crystalline structure, morphology, and porous architecture [25]. There are several polymorphic forms of Nb_2O_5 , such as monoclinic, pseudohexagonal, orthorhombic, and amorphous Nb_2O_5 forms [10]. Among polymorphs, the orthorhombic phase (T- Nb_2O_5) stands out as promising because the Li^+ ion intercalation reaction may occur both at the crystal's surface and within its interior [26]. The overall kinetics of the intercalation process in T- Nb_2O_5 were unaffected by the solid-state diffusion of Li ions due to the mostly empty octahedral sites between (001) planes [27]. As a result, the T- Nb_2O_5 demonstrates pseudocapacitive behavior for fast Li^+ intercalation and reversible and quick electrochemical kinetics [16,28,29]. According to evidence, the T- Nb_2O_5 had the highest capacity for charge storage. Researchers have studied a variety of T- Nb_2O_5 nanostructures as anodes for LIBs, including nanorods [17], nanobelts [24,30], micro flowers [25], nanowires [26], nanofibers [31], hollow spheres [32], urchins [21], nanobelts [27], nanofilms [28], microspheres [22] and so forth. Among them, mesoporous nanostructures are more appealing due to their vast surface area and multiple paths for lithium-ion transport [2].

Several fabrication approaches have been used to create mesoporous Nb_2O_5 [33]. Using a graphene-silica nanosheet template assisted by the vapour hydrolysis method at 600 °C, Wang et al. synthesized mesoporous Nb_2O_5 nanosheets with pores ranging from 3 to 20 nm [14]. Li et al., made the mesoporous Nb_2O_5 using template procedures and annealed it in air to produce non-uniform macropores of about 200 nm [19]. Using a sophisticated template process, Chen et al. created mesoporous Nb_2O_5 with pore sizes ranging from 4.3 to 7.5 nm [34]. Using three-step oxidation phases, Kong et al. created a mesoporous $Nb_2O_5@carbon$ core-shell structure with pore diameters of 2–3 nm [30]. Recently, Pligovka et al., employed highly sophisticated and advanced techniques such as successive sputtering and sequential anodization followed by potentiodynamic re-

anodization to fabricate niobium oxide nanocolumns with modulated diameters onto Al/Nb bilayer specimen silicon wafer [35] and skittle-, medusa-, and goblet-like niobia embryos onto Al/Nb bilayer specimen silicon wafer [36]. Using these methods to generate mesoporous structures are inherently time-consuming, challenging and need a specialized template. Therefore, finding a quick and effective approach to prepare a porous T-Nb₂O₅ is still challenging. A sol-gel approach was chosen to prepare T-Nb₂O₅ nanoparticles because of its low working temperatures and the ability to make consistent particle sizes (i.e., significant control of particle sizes) with specific morphologies, as well as the ease of carrying out experiments compared to other synthesis methods [37,38]. It is a standard, commercial, and economical approach to modifying the texture of substrates using the sol-gel technique.

In this study, we report the synthesis of mesoporous T-Nb₂O₅ nanoparticles by heating the peroxy niobic acid sol (Nb₂(O₂)₂O₃·6H₂O), produced by peptizing the niobic acid precipitate with aqueous H₂O₂ solution. The structural characteristics and charge-discharge performance of Nb₂O₅ were investigated using a combination of physicochemical and electrochemical techniques. The synthesized Nb₂O₅ crystallized in the orthorhombic phase and exhibited a nanoparticle shape with enhanced specific surface area (65 m² g⁻¹). The T-Nb₂O₅ displayed a high discharge capacity and improved rate capability, a remarkable cycle life (70% capacity retention) and an average CE of 98% over 300 cycles.

2. Materials and Methods

2.1. Synthesis of Nb₂O₅ Nanoparticles

Niobium (V) oxide (Nb₂O₅) nanoparticles have been produced using a previously disclosed method [38]. Under vigorous stirring, 0.5 g of niobium pentachloride (NbCl₅, 99%, Alfa Aesar) powder was dissolved in 2 mL of ethanol solution (EtOH, 99.5%, Alfa Aesar) and left until a clear NbCl₅ EtOH yellow solution appeared. By dropwise addition of 20 mL aqueous ammonia solution (0.3 M), a white-coloured precipitate of niobic acid (Nb₂O₅·nH₂O) emerged from this solution. The residue was centrifuged and rinsed with deionized water numerous times. The resultant solid product of Nb₂O₅·nH₂O precursor was then dispersed in 10 mL of 30 wt% H₂O₂ (Merck Chemicals) and agitated for 5 min in an ice bath, yielding a transparent yellow-sol (from now on referred to as “peroxy niobic acid sol, (Nb₂(O₂)₂O₃·6H₂O)”). This sol was transferred to a 20 mL autoclave and baked at 80 °C for 48 h. The resultant product was dried and sintered at 700 °C for 3 h at a heating rate of 5 °C/min to generate T-Nb₂O₅ nanoparticles.

2.2. Materials Characterization

Thermogravimetric analysis (TGA) and differential thermal analysis (DTA) of the precursor were done in air using thermal analysis (TA) in a TGAQ500V20.10 Build 36 instrument from 25 to 800 °C with a heating rate of 20 °C min⁻¹. The X-ray diffraction (XRD) studies were performed on a Rigaku Ultima IV powder X-ray diffractometer equipped with a Ni-filtered Cu K α radiation source. To get the lattice parameters and structural parameters, the resulting XRD data was refined using Rietveld analysis using the GSAS software program. Scanning electron microscopy (FESEM; FEI, Quanta 400; SEMTech Solutions, Inc., North Billerica, MA, USA), transmission electron microscopy (TEM, JOEL JEM 3010; JEOL Ltd., Freising, Germany), and high-resolution TEM examinations were undertaken to expose the sample shape and structure. Prior to TEM examinations, the sample powder was diluted in ethanol using a sonicator before being drop-cast onto a Cu grid and vacuum dried. Nitrogen adsorption-desorption measurements were studied at 77 K with a Micromeritics ASAP 2020 physisorption tool. Before determining the isotherm, the sample was degassed in a vacuum for 12 h at 150 °C. The BET (Brunauer-Emmett-Teller) model was used to compute the specific surface area. The Barrett-Joyner-Halenda (BJH) approach was used to estimate the pore-size distribution curve based on the isotherm’s desorption branch. The maximum position in the pore-size distribution was used to calculate the pore diameter. X-ray photoelectron spectroscopy (XPS) spectra were taken at the core-level using Omicron

Nanotechnology equipment and a monochromatic Mg K α ($h\nu = 1253.6$ eV) radiation source. The binding energy (BE) was calibrated using containment carbon (C1s = 284.5 eV).

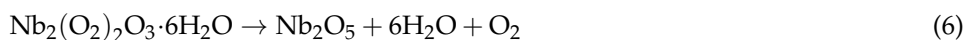
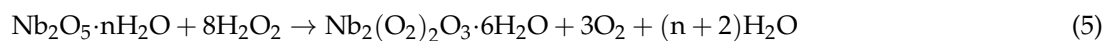
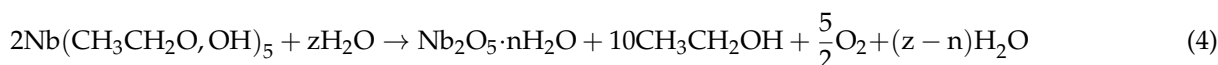
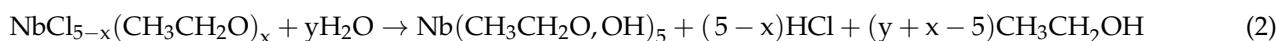
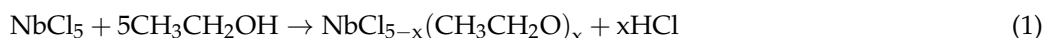
2.3. Electrochemical Measurements

The electrochemical properties of mesoporous T-Nb₂O₅ were studied using galvanostatic cycling in a CR2025-type coin cell. The active component (T-Nb₂O₅) was blended with acetylene black and the binder (polyvinylidene fluoride, PVDF, soaked in N-methyl pyrrolidinone) in a 75:15:10 weight ratio. Using a doctor blade, the slurry was then evenly applied to Cu-disk current collectors. After that, the electrodes were vacuum-dried overnight at 80 °C. The loading density of electroactive substances was approximately 1.5 mg cm⁻². In an argon-filled glove box (both moisture and oxygen levels were 0.3 ppm), the electrodes were assembled in CR2025 coin cells. The reference and counter electrodes were Li metal, whereas the separator was a porous polypropylene membrane (Celgard 2500; Celgard, Charlotte, NC, USA). The Celgard 2500 separator had a porosity of 55% and an average pore size of 28 nm. The electrolyte was a 1:1 v/v mixture of EC and DMC solvents. A LAND battery test device was used to measure the galvanostatic charge-discharge (GCD) performance of the coin cells'. Electrochemical data from cyclic voltammetry (CV; 1–3 V) and impedance spectroscopy were recorded using a Versa-STAT MC multichannel potentiostat/galvanostat electrochemical workstation (Princeton Applied Research).

3. Results and Discussion

3.1. Structural Characterizations

Based on literature reports [39,40], we described a possible reaction process for the synthesis of T-Nb₂O₅ which includes the following steps: (i) precipitation of niobic acid (Equations (1)–(4)), (ii) formation of peroxy niobic acid sol (Equation (5)), and (iii) formation of T-Nb₂O₅ by thermal annealing of the peroxy niobic acid sol at 700 °C (Equation (6)):



TGA and DTG analysis was used to estimate the weight loss of Nb₂(O₂)₂O₃·6H₂O precursor with temperature, as shown in Figure 1. The steady weight loss that was seen up to 450 °C and the weight loss recorded below 100 °C were caused by the removal of adsorbed water molecules. The weight loss seen in multiple stages between 100 and 400 °C is ascribed to the loss of crystalline water and the pyrolysis of “peroxy niobic acid sol” due to the creation of the Nb₂O₅ phase [22]. No discernible weight loss between 400 and 700 °C indicates that Nb₂O₅ nanoparticles crystallize at these temperatures. Thus, a sintering temperature of 700 °C was chosen to synthesize T-Nb₂O₅ nanoparticles. The Nb ions in the T-Nb₂O₅ crystal structure coordinate with six or seven oxygen ions, generating highly deformed octahedral (NbO₆) and pentagonal bipyramidal (NbO₇) frameworks. These polyhedra were linked together via edge- or corner-sharing in the ab-plane and corner-sharing along the c-axis, resulting in a framework similar to the “room and pillar” [41,42]. The distinctive “room-and-pillar” NbO₆/NbO₇ framework structure can offer a stable host as well as simple diffusion pathways for Li intercalation [43].

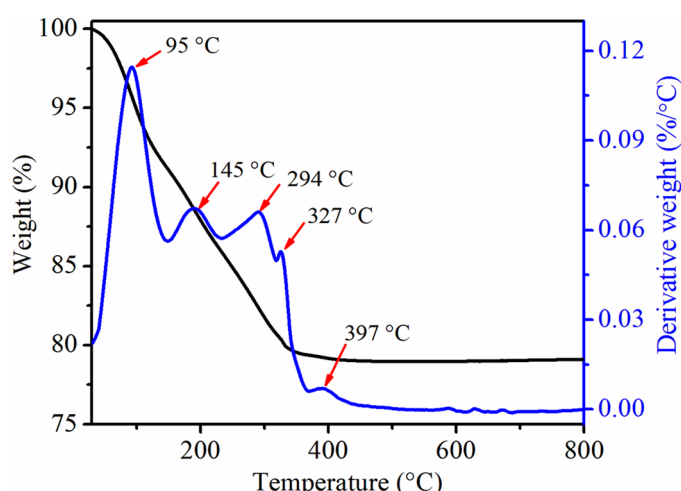


Figure 1. TGA and DTA of the as-synthesized peroxy niobic acid sol precursor.

The XRD pattern of uncalcined peroxy niobic acid precursor powder reveals wide diffraction peaks (Figure 2B), showing that the substance is amorphous in nature. The material clearly shows crystalline diffraction peaks after annealing the precursor powder at 700 °C, which is indexed to orthorhombic Nb₂O₅ (T-Nb₂O₅, space group: *Pbam*). It is worth noting that the absence of additional diffraction peaks implies that the produced orthorhombic Nb₂O₅ is of excellent purity. The Rietveld refinement approach was then used to investigate the crystalline phase development and lattice properties of T-Nb₂O₅. The experimental results and the X-ray Rietveld refinement based on the orthorhombic phase are shown in Figure 2C. The structure refinement parameters are $R_p = 5.0\%$, $R_{wp} = 6.5\%$, and $\chi^2 = 6.9$, respectively. The lowered χ^2 indicates that the X-ray Rietveld refinement exercise fits the experimental data well. The refined lattice constants are $a = 6.142$, $b = 29.119$, $c = 3.908$ and $V = 707.29 \text{ \AA}^3$; these values agree with the literature [42]. SEM and TEM examinations were used to study the surface shape and structure of the sample (Figure 3). Figure 3A,B show that all the particles in the T-Nb₂O₅ sample were agglomerated and have an interlocking porous structure. The TEM image (Figure 3C) reveals a uniform distribution of nanoparticles with dimensions ranging from 20 to 25 nm, and the particles are agglomerated. The lattice fringe spacing in the high-resolution TEM (Figure 3D) is 0.386 nm, corresponding to the (001) plane of T-Nb₂O₅.

The surface textural characteristics of the as-prepared T-Nb₂O₅ were determined by implementing nitrogen sorption isotherms at 77 K using nitrogen adsorbent. As seen from Figure 4A, the T-Nb₂O₅ isotherm exhibits a typical type IV with a clear H3-type hysteresis loop (based on IUPAC classification) [44] with a broad capillary condensation range starting at high relative pressures (P/P_0) of 0.4 and extending to 0.8, demonstrating that the mesoporous characteristic of the sample gives rise to a relatively high specific surface area of $65 \text{ m}^2 \text{ g}^{-1}$ and pore volume of $0.135 \text{ cm}^3 \text{ g}^{-1}$. The BJH approach was used to analyze the pore-size distribution (Figure 4B). The sample's pore-size-distribution curve shows a bimodal pore-size distribution, with most pores constituted of micropores and mesopores less than 3.5 nm and an average pore width of 2.20 nm, representing mesoporous characteristics. It is worth mentioning that the computed BET-specific surface area of our T-Nb₂O₅ nanoparticles is much greater than that of previously reported Li-ion battery anodes [22,23,27,31] and Li-selective adsorbates [45–48]. The high specific surface area, large pore volume, and critical micro- and mesopores of T-Nb₂O₅ would be advantageous because they provide many electro-active sites for the uptake and release of Li⁺ ions from the electrolyte during repeated charge-discharge cycling. As a result, T-Nb₂O₅ nanoparticles greatly improved battery performance, including high specific capacity and high cycle stability.

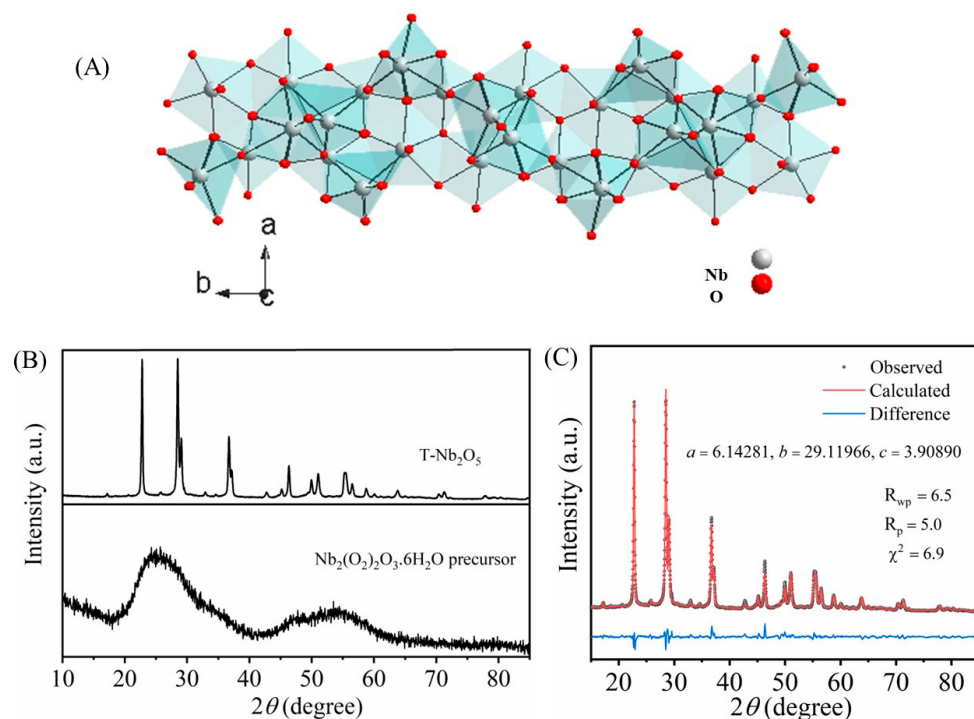


Figure 2. (A) Crystallographic structures of $T\text{-Nb}_2\text{O}_5$ (orthorhombic, S.G. $Pbam$); (B) Comparison of XRD patterns of $\text{Nb}_2(\text{O}_2)_2\text{O}_3\cdot 6\text{H}_2\text{O}$ precursor and $T\text{-Nb}_2\text{O}_5$. (C) Rietveld refined XRD pattern of the $T\text{-Nb}_2\text{O}_5$.

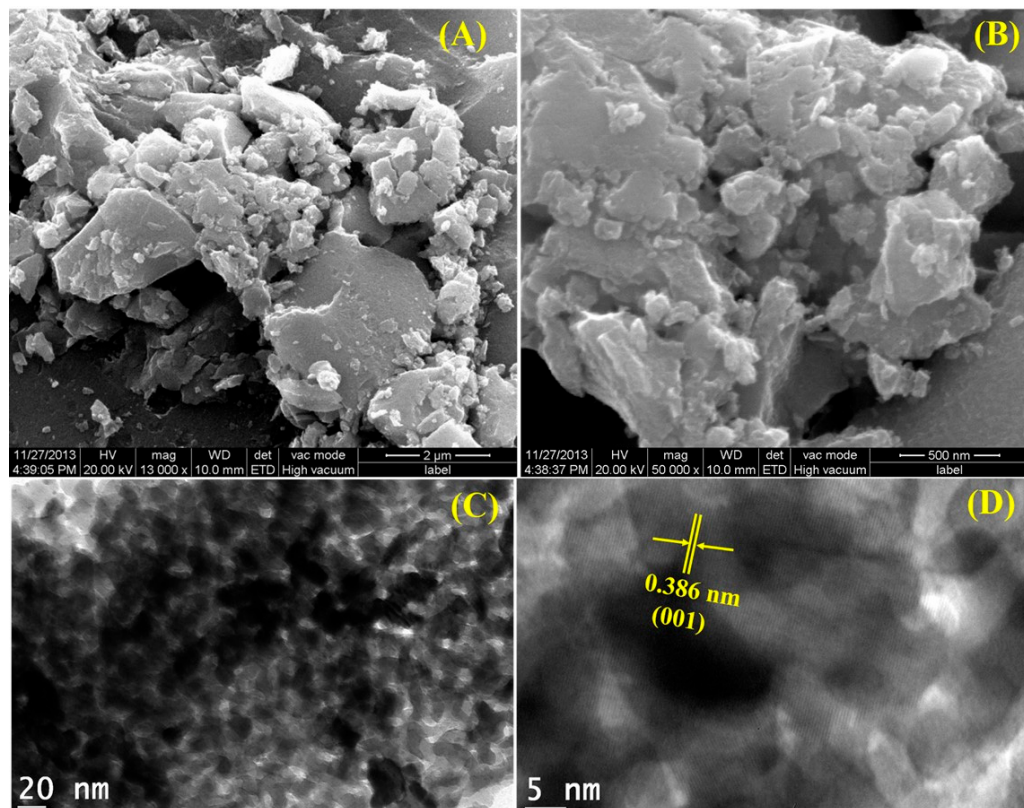


Figure 3. Different magnified SEM (A,B) and TEM (C,D) images of orthorhombic $T\text{-Nb}_2\text{O}_5$.

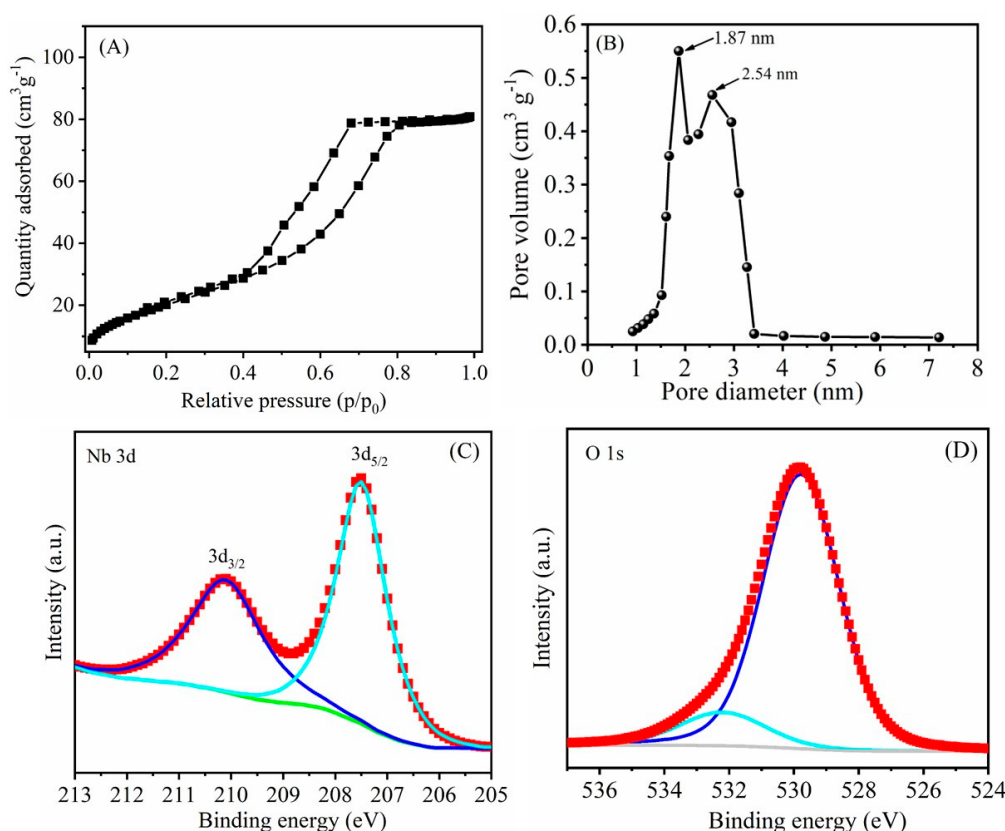


Figure 4. (A) Nitrogen adsorption-desorption isotherm at 77 K and (B) BJH pore size distribution analysis of T–Nb₂O₅. High-resolution XPS spectra of (C) Nb 3d and (D) O 1s for the T–Nb₂O₅.

XPS was used to evaluate the surface elemental compositions and chemical states of metal ions in T–Nb₂O₅. XPS is a popular non-destructive technology for identifying the chemical states of metal and nonmetal ions that are commonly utilized in investigating Li-ion battery electrode materials. Due to the strong spin-orbit splitting, the high-resolution XPS spectra of Nb 3d (Figure 4C) exhibit two unique peaks centered at BE of 207.5 eV for Nb 3d_{5/2} and 210.2 eV for Nb 3d_{3/2} [23]. The BE values agreed with the literature and verified that the bulk of the Nb element in the synthesized material is mostly Nb⁵⁺ with minimal Nb⁴⁺, owing to surface reduction at high temperatures [33,39]. Figure 4D shows the deconvolution of the O 1s XPS spectra into two peaks. The strong peak at BE of 529.8 eV corresponds to O-Nb, while the peak at 532.1 eV belongs to adsorbed oxygen [39,41].

3.2. Electrochemical Studies

To evaluate the electrochemical performance of Li⁺ ion intercalation into or deintercalation from mesoporous T–Nb₂O₅, coin cell-based batteries were assembled with mesoporous T–Nb₂O₅ as the working electrode and Li foil as the counter and reference electrodes. Figure 5A represents the initial three sequential CV curves of the T–Nb₂O₅ electrode collected at a sweep rate of 5 mV s⁻¹ within the applied potential window of 1.0–3.0 V (vs. Li⁺/Li). Three CV curves overlap nicely and reveal excellent reversibility of Li-storage characteristics. Furthermore, the shape of the CV curves reveals a prominent redox response with a couple of broad redox peaks within the applied potential range due to Li⁺ insertion/extraction and the redox of niobium ions i.e., Nb⁵⁺↔Nb⁴⁺ and Nb⁴⁺↔Nb³⁺, according to the eqn. Nb₂O₅ + xLi⁺ + xe⁻ → Li_xNb₂O₅ ($x \leq 2$) [6,49–51].

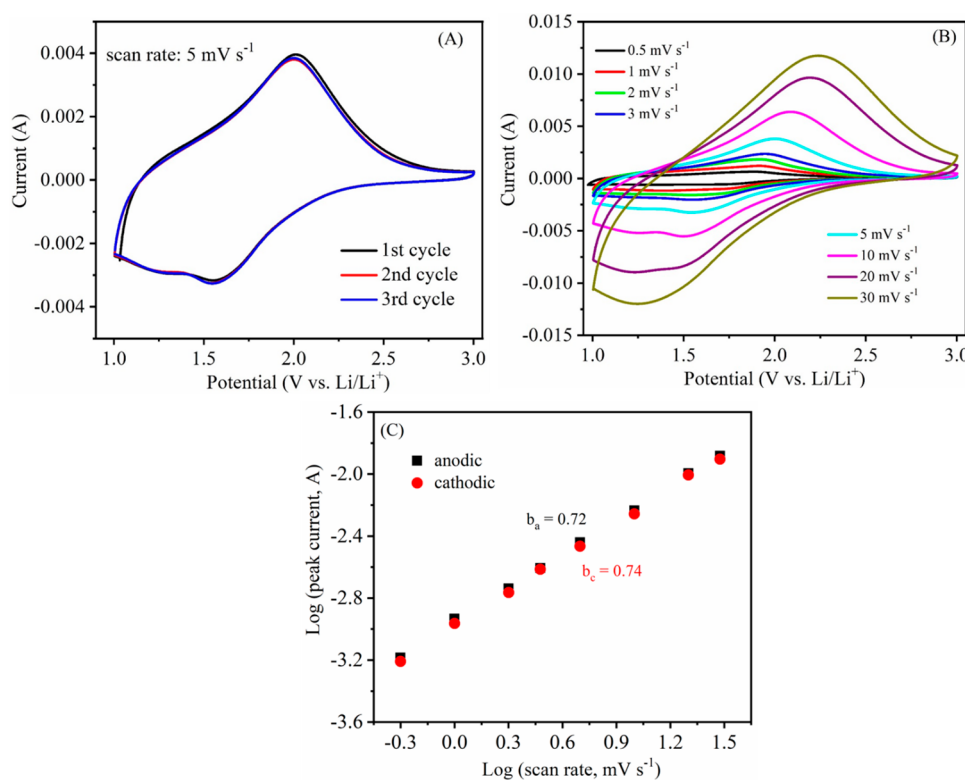


Figure 5. Electrochemical characteristics of the T–Nb₂O₅: (A) CV profiles of the first three cycles; (B) CV profiles at different sweep rates ranging from 0.5 to 30 mV s^{−1}, and (C) corresponding logarithmic relationships between the scan rates and peak currents.

To further evaluate the electrochemical kinetic characteristics of the mesoporous T–Nb₂O₅ electrode, CV curves were generated at various sweep rates ranging from 0.5 to 30 mV s^{−1} (Figure 5B). Peak currents (both anodic and cathodic) vary drastically as the scan rate increases, owing to diffusion-controlled ohmic contributions [39,50]. The kinetic information of the Li⁺ intercalation can be obtained by the relationship between the peak current (*i*) vs. sweep rate (ν , mV/s) [6,52–54]:

$$i = a\nu^b$$

where *a* denotes the variable parameter and *b* is the parameter linked with the charge storage mechanism, which may be obtained by calculating the slope of the log (*i*) vs. log (ν) plot. Usually, the *b* = ~0.5 indicates the electrochemical process is a diffusion-controlled and battery-type reaction, and the *b* = ~1 represents a surface-controlled pseudocapacitive. The *b*-values (Figure 5C) were calculated to be ~0.74 and ~0.72, respectively. For both anodic and cathodic peaks, this suggests a contribution from both the diffusion and capacitive processes.

The discharging-charging performance of the mesoporous T–Nb₂O₅ electrode was assessed via GCD measurements between 1.0 and 3.0 V (Figure 6). Figure 6A depicts typical GCD patterns for the first ten cycles of the T–Nb₂O₅ electrode at 100 mA g^{−1}. Similar to some other reports [22,39,48], all of the GCD curves exhibit a smooth sloping profile, attributable to the change of Nb₂O₅ ↔ Li_xNb₂O₅, a characteristic of insertion-type electrochemical reactions. At the beginning of discharging, it exhibits a discharging capacity as high as 225 mAh g^{−1}. With an initial charging capacity of 180 mAh g^{−1}, the T–Nb₂O₅ electrode had 80% initial CE, however, it lost some of its capacity. The subsequent (from the second to the tenth) cycle discharge capacities were 190, 183, 180, 178, 177, 177.6, 178, 178, and 179 mAh g^{−1}, respectively. The high discharge capacity and low CE of the first cycle may be caused by the formation of SEI film on the electrode surface [29].

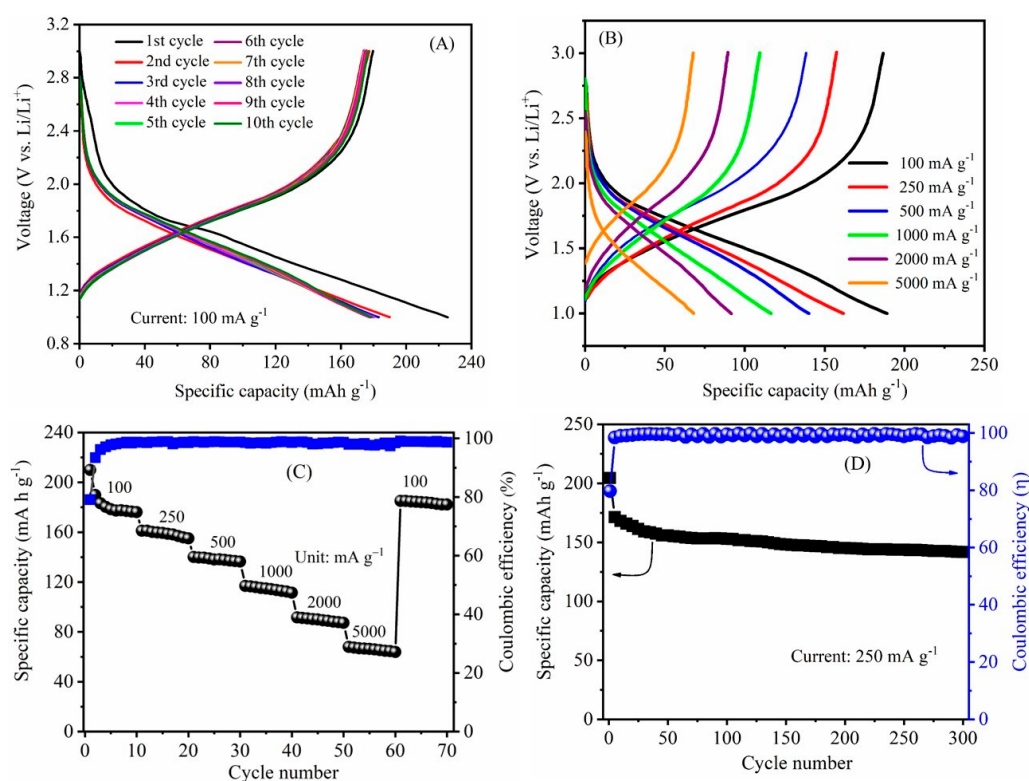


Figure 6. (A) Typical charging-discharging profiles at 100 mA g^{-1} for the first ten cycles, (B) the charging and discharging curves at different current rates, (C) the rate performance, and (D) the cycle performance at 250 mA g^{-1} for the T-Nb₂O₅ electrode.

The as-prepared T-Nb₂O₅ GCD profiles of the electrode at different current densities ranging from 100 to 5000 mA g^{-1} are shown in Figure 6B. It is evident that as the current density increases, the discharge curves drop and the charge curves rise, indicating an increase in polarization. It is evident that as current density increases the discharge curves drop and the charge curves rise, indicating that the polarization is increased. Surprisingly, the mesoporous T-Nb₂O₅ nanoparticles electrode can operate smoothly even at a high applied current density of 5 A g^{-1} ; nevertheless, there is some noticeable capacity loss at high current densities. The gradual evolution of charging-discharging voltage profiles suggests that T-Nb₂O₅ remains in a stable structure even after repeated discharging-charging cycling. Figure 6C depicts the discharge capacity of the T-Nb₂O₅ electrode as a function of current density. The graph clearly shows how the electrode's capacity rapidly degrades as the applied current density increases. At high current densities, this is usually caused by the sluggish diffusion of Li⁺ into the T-Nb₂O₅ interior [16,55,56]. The discharge capacity could be restored to its initial condition after a series of rate tests when the current density was reversed back to 100 mA g^{-1} , demonstrating that the T-Nb₂O₅ electrode possessed significant reversibility.

For the development of Li-ion batteries to be used in practical applications, the electroactive materials must exhibit long-term cycle stability. To study the long-cycle retention properties in more detail, the T-Nb₂O₅ electrode was exposed to a GCD test at 0.25 A g^{-1} in a potential window of 1.0 to 3.0 V (Li/Li⁺) for up to 300 cycles (Figure 6D). The electrode gradually lost capacity with increasing cycle number and maintained a discharge capacity of 142 mAh g^{-1} (70%) even at the end of 300 cycles. Meanwhile, the cell continued a high average CE of 98% over 300 cycles. It is worth noting that the performance of T-Nb₂O₅ in terms of its specific capacity, cyclability, and rate capability is comparable and even superior to that reported for other T-Nb₂O₅ nanostructures [22,24,25,41]. The enormous specific surface area, mesoporous structure, and nanoparticle shape of T-Nb₂O₅ improve performance because they can offer a large number of electroactive sites for the uptake and

release of Li^+ ions from the electrolyte and also shorten the diffusion distance for both the ions and electrons.

To further examine the electrochemical kinetics of the Li intercalation/deintercalation process within the T- Nb_2O_5 electrode, an AC impedance measurement was performed at OCV in the frequency range of 0.01 Hz–1 M Hz. As seen in Figure 7, the Nyquist plot (imaginary part, Z'' vs. real part, Z') of the electrode consists of a high-frequency semicircle followed by a low-frequency spike. Using the RelaxIS program, the resultant impedance data was suitably matched to an equivalent circuit illustrated in the inset of Figure 7. In the equivalent circuit, R_s ($\sim 2.45 \Omega$) indicates the electrolyte solution resistance, which can be calculated from the x-intercept of the beginning curve in the high-frequency region, and CPE ($\sim 35 \mu\text{F}$) represents the constant phase element corresponding to the double-layer capacitance [48,56]. A semicircle in the middle-frequency region shows the interfacial charge transfer resistance ($R_{ct} = 181.79 \Omega$). In contrast, the Warburg resistance ($Z_w = 0.36 \Omega \text{ s}^{-1/2}$) quantifies the diffusion of Li ions and is represented by an inclined low-frequency line [57]. A spike in the low-frequency describes the Li^+ intercalation or deintercalation behavior of the electrode.

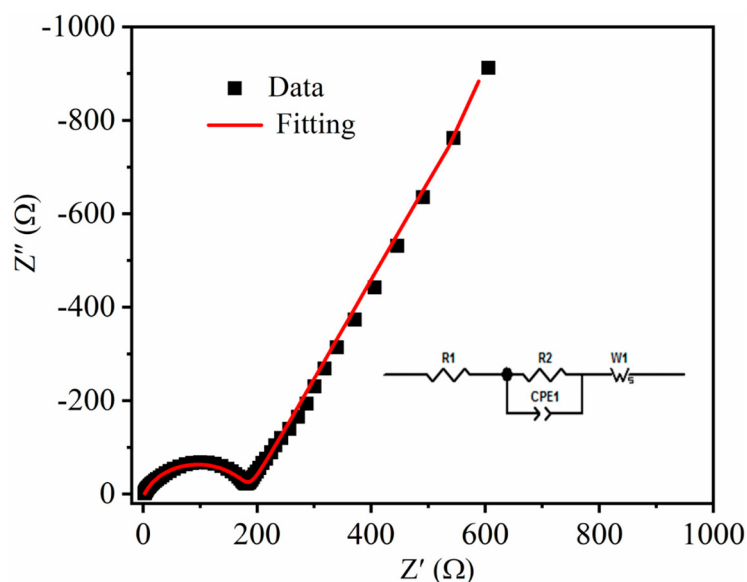


Figure 7. EIS Nyquist plots of the T- Nb_2O_5 electrode.

4. Conclusions

In conclusion, we detailed the synthesis of hierarchical mesoporous T- Nb_2O_5 nanoparticles by heating the peroxy niobic acid sol formed by peptizing the niobic acid precipitate with an aqueous H_2O_2 solution. The as-prepared electrode containing T- Nb_2O_5 nanoparticles had a high BET-specific surface area ($65 \text{ m}^2 \text{ g}^{-1}$) and good Li intercalation characteristics. The T- Nb_2O_5 electrode had a high specific capacity of 68 mAh g^{-1} at 5 A g^{-1} , remarkable cycling stability over 300 cycles (with 70% capacity retention), and potential high-rate performance. Furthermore, kinetic analysis reveals that a pseudocapacitive mechanism dominates energy storage at a high rate. Because of their unique structure and shape, mesoporous T- Nb_2O_5 nanoparticles exhibit outstanding electrochemical properties. They have a short Li ion transport channel and a wide contact area between the active material and electrolyte. Consequently, T- Nb_2O_5 nanoparticles are a suitable material for Li-ion interaction electrodes.

Author Contributions: Conceptualization, E.U. and M.S.; methodology, E.U.; software, M.S.; validation, M.S.; formal analysis, M.S. and V.P.; investigation, E.U. and G.K.; data curation, E.U.; writing—original draft preparation, E.U. and D.V.; writing—review and editing, E.U., G.K., M.S. and P.J.; supervision, E.U. All authors have read and agreed to the published version of the manuscript.

Funding: This research received no external funding.

Data Availability Statement: Not applicable.

Acknowledgments: We gratefully thank IIT Madras SAIF (sophisticated analytical instruments facility) and metallurgical departments for providing instruments for the sample analysis. Also, we would like to thank Xiamen University, China for providing electrochemical instruments to study the battery analysis.

Conflicts of Interest: The authors declare no conflict of interest.

References

1. Armand, M.; Tarascon, J. Building better batteries. *Nature* **2008**, *451*, 652–657. [[CrossRef](#)] [[PubMed](#)]
2. Yan, L.; Ruic, X.; Chen, G.; Xu, W.; Zoua, G.; Luo, H. Recent advances in nanostructured Nb-based oxides for electrochemical energy storage. *Nanoscale* **2016**, *8*, 8443–8465. [[CrossRef](#)]
3. Bruce, P.G.; Freunberger, S.A.; Hardwick, L.J.; Tarascon, J.-M. Li-O₂ and Li-S batteries with high energy storage. *Nat. Mater.* **2012**, *11*, 19–30. [[CrossRef](#)]
4. Goodenough, J.B. Electrochemical energy storage in a sustainable modern society. *Energy Environ. Sci.* **2014**, *7*, 14–18. [[CrossRef](#)]
5. Environ, E.; Etacheri, V.; Marom, R.; Salitraa, G.; Aurbach, D. Challenges in the development of advanced Li-ion batteries: A review. *Energy Environ. Sci.* **2011**, *4*, 3243–3262.
6. Augustyn, V.; Come, J.; Lowe, M.A.; Kim, J.W.; Taberna, P.-L.; Tolbert, S.H.; Abruna, H.D.; Simon, P.; Dunn, B. High-rate electrochemical energy storage through Li⁺ intercalation pseudocapacitance. *Nat. Mater.* **2013**, *12*, 518–522. [[CrossRef](#)] [[PubMed](#)]
7. Choi, C.; Ashby, D.S.; Butts, D.M.; DeBlock, R.H.; Wei, Q.L.; Lau, J.; Dunn, B. Achieving high energy density and high power density with pseudocapacitive materials. *Nat. Rev. Mater.* **2020**, *5*, 5–19. [[CrossRef](#)]
8. Umeshbabu, E.; Justin, P.; Rao, G.R. Tuning the surface morphology and pseudocapacitance of MnO₂ by a facile green method employing organic reducing sugars. *ACS Appl. Energy Mater.* **2018**, *1*, 3654–3664. [[CrossRef](#)]
9. Konda, S.; Chidurala, S.C. Applied surface science advances the impact of hybridization on specific capacitance in hybrid NiO/V₂O₅@graphene composites as advanced supercapacitor electrode materials. *Appl. Surf. Sci. Adv.* **2022**, *12*, 100329.
10. Shireesha, K.; Divya, V.; Pranitha, G.; Ashok, C.; Shilpa, C.C.; Himabindu, V. A systematic investigation on the effect of reducing agents towards specific capacitance of NiMg@OH/reduced graphene oxide nanocomposites. *Mater. Technol.* **2022**, *37*, 1864–1876.
11. Yun, Y.S.; Cho, S.Y.; Shim, J.; Kim, B.H.; Chang, S.J.; Baek, S.J.; Huh, Y.S.; Tak, Y.; Park, Y.W.; Park, S.; et al. Microporous carbon nanoplates from regenerated silk proteins for supercapacitors. *Adv. Mater.* **2013**, *25*, 1993–1998. [[CrossRef](#)] [[PubMed](#)]
12. Manthiram, A. An Outlook on lithium ion battery technology. *ACS Cent. Sci.* **2017**, *3*, 1063–1069. [[CrossRef](#)]
13. Cabana, J.; Monconduit, L.; Larcher, D.; Palacín, M.R. Beyond intercalation-based Li-ion batteries: The state of the art and challenges of electrode materials reacting through conversion reactions. *Adv. Mater.* **2010**, *22*, E170–E192. [[CrossRef](#)] [[PubMed](#)]
14. Nakazawa, H.; Sano, K.; Abe, T.; Baba, M.; Kumagai, N. Charge-discharge characteristics of all-solid-state thin-filmed lithium-ion batteries using amorphous Nb₂O₅ negative electrodes. *J. Power Sources* **2007**, *174*, 838–842. [[CrossRef](#)]
15. Arunkumar, P.; Ashish, A.G.; Babu, B.; Sarang, S.; Suresh, A.; Sharma, C.H.; Thalakulam, M.; Shajumon, M.M. Nb₂O₅/graphene nanocomposites for electrochemical energy storage. *RSC Adv.* **2015**, *5*, 59997–60004. [[CrossRef](#)]
16. Lübke, M.; Sumboja, A.; Johnson, I.D.; Brett, D.J.L.; Shearing, P.R.; Liu, Z.; Darr, J.A. High power nano-Nb₂O₅ negative electrodes for lithium-ion batteries. *Electrochim. Acta* **2016**, *192*, 363–369. [[CrossRef](#)]
17. Cao, K.; Jin, T.; Yang, L.; Jiao, L. Recent progress in conversion reaction metal oxide anodes for Li-ion batteries. *Mater. Chem. Front.* **2017**, *1*, 2213–2242. [[CrossRef](#)]
18. Poizot, P.; Laruelle, S.; Grugéon, S.; Dupont, L.; Tarascon, J.-M. Nanosized transition-metaloxides as negative-electrode materials for lithium-ion batteries. *Nature* **2000**, *407*, 496–499. [[CrossRef](#)]
19. Zhang, H.; Yang, Y.; Xu, H.; Wang, L.; Lu, X.; He, X. Li₄Ti₅O₁₂ spinel anode: Fundamentals and advances in rechargeable batteries. *InfoMat* **2022**, *4*, e12228. [[CrossRef](#)]
20. Zhang, Y.; Tang, Y.; Liu, L.; Zhang, Y.; Li, Z. T-Nb₂O₅ nanoparticles confined in carbon nanotubes with fast ion diffusion rates for lithium storage. *Dalton Trans.* **2021**, *50*, 14532–14536. [[CrossRef](#)]
21. Yi, T.-F.; Sari, H.M.K.; Li, X.; Wang, F.; Zhu, Y.-R.; Hu, J.; Zhang, J.; Li, X. A review of niobium oxides based nanocomposites for lithium-ion batteries, sodium-ion batteries and supercapacitors. *Nano Energy* **2021**, *85*, 105955. [[CrossRef](#)]
22. Liu, G.; Jin, B.; Bao, K.; Xie, H.; Guo, J.; Ji, X.; Zhang, R.; Jiang, Q. Facile synthesis of porous Nb₂O₅ microspheres as anodes for lithium-ion batteries. *Int. J. Hydrogen Energy* **2017**, *42*, 6065–6071. [[CrossRef](#)]
23. Yang, H.; Xu, H.; Wang, L.; Zhang, L.; Huang, Y.; Hu, X. Microwave-assisted rapid synthesis of self-assembled T-Nb₂O₅ nanowires for high-energy hybrid supercapacitors. *Chem. Eur. J.* **2017**, *23*, 4203–4209. [[CrossRef](#)]
24. Liu, X.; Liu, G.; Chen, H.; Ma, J.; Zhang, R. Facile synthesis of Nb₂O₅ nanobelts assembled from nanorods and their applications in lithium ion batteries. *J. Phys. Chem. Solids* **2017**, *111*, 8–11. [[CrossRef](#)]
25. Chen, J.; Wang, H.; Zhang, X.; Liu, B.; Xu, L.; Zhang, Z.; Zhang, Y. 2D ultrathin nanosheet-assembled Nb₂O₅ microflowers for lithium ion batteries. *Mater. Lett.* **2018**, *227*, 112–115. [[CrossRef](#)]

26. Song, H.; Fu, J.; Ding, K.; Huang, C.; Wu, K.; Zhang, X.; Gao, B.; Huo, K.; Peng, X.; Chu, P.K. Flexible Nb₂O₅ nanowires/graphene film electrode for high-performance hybrid Li-ion supercapacitors. *J. Power Sources* **2016**, *328*, 599–606. [CrossRef]
27. Huang, C.; Fu, J.; Song, H.; Li, X.; Peng, X.; Gao, B.; Zhang, X.; Chu, P.K. General fabrication of mesoporous Nb₂O₅ nanobelts for lithium ion battery anodes. *RSC Adv.* **2016**, *6*, 90489–90493. [CrossRef]
28. Kong, L.; Liu, X.; Wei, J.; Wang, S.; Xu, B.B.; Long, D.; Chen, F. T-Nb₂O₅ nanoparticle enabled pseudocapacitance with fast Li-ion intercalation. *Nanoscale* **2018**, *10*, 14165–14170. [CrossRef]
29. Lin, J.; Yuan, Y.; Su, Q.; Pan, A.; Dinesh, S.; Peng, C.; Cao, G.; Liang, S. Facile synthesis of Nb₂O₅/carbon nanocomposites as advanced anode materials for lithium-ion batteries. *Electrochim. Acta* **2018**, *292*, 63–71. [CrossRef]
30. Wei, M.; Wei, K.; Ichihara, M.; Zhou, H. Electrochemistry communications Nb₂O₅ nanobelts: A lithium intercalation host with large capacity and high rate capability. *Electrochem. Commun.* **2008**, *10*, 980–983. [CrossRef]
31. Cheong, J.Y.; Jung, J.-W.; Youn, D.-Y.; Kim, C.; Yu, S.; Cho, S.-H.; Yoon, K.R.; Kim, I.-D. Mesoporous orthorhombic Nb₂O₅ nanofibers as pseudocapacitive electrodes with ultra-stable Li storage characteristics. *J. Power Sources* **2017**, *360*, 434–442. [CrossRef]
32. Sasidharan, M.; Gunawardhana, N.; Yoshio, M.; Nakashima, K. Nb₂O₅ hollow nanospheres as anode material for enhanced performance in lithium ion batteries. *Mater. Res. Bull.* **2012**, *47*, 2161–2164. [CrossRef]
33. Meng, J.; He, Q.; Xu, L.; Zhang, X.; Liu, F.; Wang, X.; Li, Q.; Xu, X.; Zhang, G.; Niu, C.; et al. Identification of phase control of carbon-confined Nb₂O₅ nanoparticles toward high-performance lithium storage. *Adv. Energy Mater.* **2019**, *9*, 1802695. [CrossRef]
34. Lai, C.H.; Ashby, D.; Moz, M.; Gogotsi, Y.; Pilon, L.; Dunn, B. Designing pseudocapacitance for Nb₂O₅/carbide-derived carbon electrodes and hybrid devices. *Langmuir* **2017**, *33*, 9407–9415. [CrossRef]
35. Pligovka, A.; Zakhlebayeva, A.; Lazavenka, A. Niobium oxide nanocolumns formed via anodic alumina with modulated pore diameters. *J. Phys. Conf. Ser.* **2018**, *987*, 012006. [CrossRef]
36. Pligovka, A.; Hoha, A.; Turavets, U.; Poznyak, A.; Zakharaev, Y. Formation features, morphology and optical properties of nanostructures via anodizing Al/Nb on Si and glass. *Mater. Today Proc.* **2021**, *37*, A8–A15. [CrossRef]
37. Hu, J.J.; Li, J.J.; Wang, K.; Xia, H.Y. Self-assembly Nb₂O₅ microsphere with hollow and carbon coated structure as high rate capability lithium-ion electrode materials. *Electrochim. Acta* **2020**, *331*, 135364–135373. [CrossRef]
38. Umeshbabu, E.; Rao, G.R. High electrocatalytic activity of Pt/C catalyst promoted by TT-Nb₂O₅ nanoparticles under acidic conditions. *ChemistrySelect* **2017**, *2*, 4204–4212. [CrossRef]
39. Li, S.; Xu, Q.; Uchaker, E.; Cao, X.; Cao, G. Comparison of amorphous, pseudohexagonal and orthorhombic Nb₂O₅ for high-rate lithium ion insertion. *CrystEngComm* **2016**, *18*, 2532–2540. [CrossRef]
40. Uekawa, N.; Kudo, T.; Mori, F.; Wu, Y.J.; Kakegawa, K. Low-temperature synthesis of niobium oxide nanoparticles from peroxy niobic acid sol. *J. Colloid Interface Sci.* **2003**, *264*, 378–384. [CrossRef]
41. Yang, M.; Li, S.; Huang, J. Three-dimensional cross-linked Nb₂O₅ polymorphs derived from cellulose substances: Insights into the mechanisms of lithium storage. *ACS Appl. Mater. Interfaces* **2021**, *13*, 39501–39512. [CrossRef] [PubMed]
42. Zheng, Y.; Yao, Z.; Shadike, Z.; Lei, M.; Liu, J.; Li, C. Defect-concentration-mediated T-Nb₂O₅ anodes for durable and fast-charging Li-ion batteries. *Adv. Funct. Mater.* **2021**, *32*, 2107060. [CrossRef]
43. Rouquerol, F. *Adsorption by Powders and Porous Solids*; Academic Press: London, UK, 1999.
44. Siekierka, A. Lithium iron manganese oxide as an adsorbent for capturing lithium ions in hybrid capacitive deionization with different electrical modes. *Sep. Purif. Technol.* **2019**, *236*, 116234. [CrossRef]
45. Rozhdestvenska, L.M.; Chaban, M.O.; Dzyazko, Y.S.; Palchik, O.V.; Dzyazko, O.G. Formation of lithium-selective sorbent in nanoreactors of the support based on titanium dioxide. *Appl. Nanosci.* **2021**, *12*, 1113–1122. [CrossRef]
46. Huang, Y.; Wang, R. Green recovery of lithium from water by a smart imprinted adsorbent with photo-controlled and selective properties. *Chem. Eng. J.* **2019**, *378*, 122084. [CrossRef]
47. Griffith, K.J.; Forse, A.C.; Griffin, J.M.; Grey, C.P. High-rate intercalation without nanostructuring in metastable Nb₂O₅ bronze phases. *J. Am. Chem. Soc.* **2016**, *138*, 8888–8899. [CrossRef]
48. Luo, G.; Li, H.; Zhang, D.; Gao, L.; Lin, T. A template-free synthesis via alkaline route for Nb₂O₅/carbon nanotubes composite as pseudo-capacitor material with high-rate performance. *Electrochim. Acta* **2017**, *235*, 175–181. [CrossRef]
49. Kim, J.W.; Augustyn, V.; Dunn, B. The effect of crystallinity on the rapid pseudocapacitive response of Nb₂O₅. *Adv. Energy Mater.* **2012**, *2*, 141–148. [CrossRef]
50. Kong, L.; Zhang, C.; Wang, J.; Qiao, W.; Ling, L.; Long, D. Free-standing T-Nb₂O₅/graphene composite papers with ultrahigh gravimetric/volumetric capacitance for Li-ion intercalation pseudocapacitor. *ACS Nano* **2015**, *9*, 11200–11208. [CrossRef]
51. Krishnan, S.G.; Pham, H.D.; Mahale, K.; Nanjundan, A.K.; Dubal, D. Nanostructure-dependent electrochemical properties of Nb₂O₅ for long-life Li-ion batteries. *ACS Appl. Eng. Mater.* **2022**, *1*, 469–476. [CrossRef]
52. Come, J.; Augustyn, V.; Kim, J.W.; Rozier, P.; Taberna, P.L.; Gogotsi, P.; Long, J.W.; Dunn, B.; Simon, P. Electrochemical kinetics of nanostructured Nb₂O₅ electrodes. *J. Electrochem. Soc.* **2014**, *161*, A718–A725. [CrossRef]
53. Lou, S.; Cheng, X.; Wang, L.; Gao, J.; Li, Q.; Ma, Y.; Gao, Y.; Zuo, P.; Du, C.; Yin, G. High-rate capability of three-dimensionally ordered macroporous T-Nb₂O₅ through Li⁺ intercalation pseudocapacitance. *J. Power Sources* **2017**, *361*, 80–86. [CrossRef]
54. Chen, J.; Wang, Y.; He, X.; Xu, S.; Fang, M.; Zhao, X.; Shang, Y. Electrochemical properties of MnO₂ nanorods as anode materials for lithium ion batteries. *Electrochim. Acta* **2014**, *142*, 152–156. [CrossRef]

55. Park, J.H.; Choi, W.Y.; Lee, S.; Kim, T.-S.; Lee, J.W. Graphene intercalated free-standing carbon paper coated with MnO₂ for anode materials of lithium ion batteries. *Electrochim. Acta* **2020**, *348*, 136310. [[CrossRef](#)]
56. Umeshbabu, E.; Satyanarayana, M.; Karkera, G.; Pullamsetty, A.; Justin, P. Hierarchical a-MnO₂ nanowires as an efficient anode material for rechargeable lithium-ion batteries. *Mater. Adv.* **2022**, *3*, 1642–1651. [[CrossRef](#)]
57. Umeshbabu, E.; Rao, G.R. Vanadium pentoxide nanochains for high-performance electrochemical supercapacitors. *J. Colloid Interface Sci.* **2016**, *472*, 210–219. [[CrossRef](#)] [[PubMed](#)]

Disclaimer/Publisher's Note: The statements, opinions and data contained in all publications are solely those of the individual author(s) and contributor(s) and not of MDPI and/or the editor(s). MDPI and/or the editor(s) disclaim responsibility for any injury to people or property resulting from any ideas, methods, instructions or products referred to in the content.